Journal of Sol-Gel Science and Technology 30, 5–19, 2004

# Synthesis and Microstructural Properties of Fe-TiO$_2$ Nanocrystalline Particles Obtained by a Modified Sol-Gel Method

N. ŠIJAKOVIĆ-VUJIČIĆ
*Division of Organic Chemistry and Biochemistry, Laboratory of Supramolecular and Nucleoside Chemistry, Ruđer Bošković Institute, P.O. Box 180, HR-10002 Zagreb, Croatia*

M. GOTIĆ* AND S. MUSIĆ
*Division of Materials Chemistry, Ruđer Bošković Institute, P.O. Box 180, HR-10002 Zagreb, Croatia*
gotic@rudjer.irb.hr

M. IVANDA
*Division of Materials Physics, Ruđer Bošković Institute, P.O. Box 180, HR-10002 Zagreb, Croatia*

S. POPOVIĆ
*Department of Physics, Faculty of Science, University of Zagreb, P.O. Box 331, HR-10002 Zagreb, Croatia*

*Received March 3, 2003; Accepted January 26, 2004*

**Abstract.** A series of iron/titanium oxide nanocrystalline particles with Fe/Ti molar ratios up to 0.15 were synthesized by a modified sol-gel technique using Ti(IV)-isopropoxide and anhydrous Fe(II)-acetate. The precursors were mixed and subsequently hydrolyzed with water molecules generated *in situ* by an esterification reaction between acetic acid and ethanol. As-synthesized samples were amorphous for XRD, independently of the relative amount of doped iron. The undoped samples and samples with the molar ratio Fe/Ti $= 0.01$, treated at up to 500°C, contained anatase as the dominant phase and rutile as the minor phase. The samples with the Fe/Ti molar ratio of 0.15, treated at the same temperature, contained anatase (major phase), rutile (minor phase) and a very small amount of an unidentified phase. The crystallite size of the dominant phase in the samples was estimated from the XRD line broadening using the Scherrer formula. Thermogravimetric analysis showed that weight loss was accelerated and completed at lower temperatures as the relative concentration of iron in the Fe-TiO$_2$ samples increased. The strong exothermic peak in the DTA curve between 300 and 450°C in the undoped TiO$_2$ sample shifted to the lower temperatures and became much more asymmetrical with increased iron doping. This DTA peak corresponded to the amorphous-to-anatase-transition and it included several steps such as (i) the thermal degradation of strongly bound organic molecules, (ii) the condensation of unhydrolyzed –OR groups, (iii) the sintering and growth of particles and (iv) the rearrangement of newly formed chemical bonds. The center of the most intense Raman band of the $E_g$ mode at 143.8 cm$^{-1}$ in the undoped TiO$_2$ sample continually shifted to higher wave numbers and the full-width at half maximum increased with iron doping. Transmission electron microscopy revealed decrease of the mean particle size from 16.3 nm in undoped sample to 9.7 nm in the highest iron doped sample. The particle size distribution becomes

---

*To whom all correspondence should be addressed.

narrower with iron doping. The narrowest particle size distribution was found in sample with the Fe/Ti molar ratio of 0.05, calcined at 500°C. Scanning electron microscopy of undoped samples calcined at 580°C showed irregular aggregates having a relatively flat surface. On the contrary, the samples doped with 15 mol% of iron and treated at the same temperature exhibited a non-uniform sponge-like surface with distributed micrometer holes.

**Keywords:** Fe-$TiO_2$ particles, iron doping, sol-gel, nanocrystallinity, microstructure, esterification, DTA/TGA, Raman, TEM/SEM, XRD

## 1. Introduction

Titanium dioxide ($TiO_2$) is an important photocatalyst that has already found commercial applications due to its specific optical and electronic properties, low cost, chemical stability and non-toxicity. The main disadvantage in the practical photochemical applications of the pure $TiO_2$ phase is its relatively low absorption in the visible portion of the solar spectrum. Generally, doping of $TiO_2$ with transition metal cations was reported as a good tool to improve photocatalytic properties [1, 2] and for enhancement of visible light response [3]. Iron doped $TiO_2$ nanocrystalline particles showed better photocatalytic activity than pure $TiO_2$ in various chemical reactions such as photochemical ammonia synthesis from $N_2$ and $H_2O$ [4–6], $CCl_4$ reduction and $CHCl_3$ oxidation [7], oxidation of methanol in an aqueous solution [8] and degradation of dichloroacetic [9], formic [10] and maleic acids [11] as a model pollutants.

The homogeneity of the iron dispersion in the $TiO_2$ crystal lattice as well as the structural and photocatalytic properties of iron doped $TiO_2$ are strongly dependent on the iron precursor and the method of preparation. For example, Ranjit et al. [12] reported an enhanced activity in the degradation of organic pollutants for iron(III)-phtalocyanine modified $TiO_2$ as compared to nonmodified $TiO_2$. Rivas et al. [13] found that it is easier to obtain homogeneous samples starting with iron(II)-salt than with several different iron(III)-salts. Wang et al. [8] showed that the mixing of Ti and Fe-organic precursors before hydrolysis yielded highly active iron doped $TiO_2$ nanoparticles for the oxidation of methanol in an aqueous solution. Wang et al. [14] showed the influence of pH on the uniformity of iron distribution in Fe(III)-doped $TiO_2$ nanoparticles. The uniform solid solution of iron-titanium oxide was formed at pH 6.0 using the hydrothermal method. Kato et al. [15] showed that the traces of water in commercial absolute ethanol could influence the pore size and crystallographic orientation of anatase coatings on quartz-glass plates.

An iron doped $TiO_2$ system is of a complex nature and its investigation is also important from the structural standpoint [16–24]. The structural complexity of an iron doped $TiO_2$ system arises from the low solubility limit of iron ions in anatase and rutile, from anatase/brookite to rutile transition at higher temperatures, and from the appearance of pseudobrookite at higher temperatures and iron loading. Hematite [14, 18, 21, 22, 25–27] and, in only a few cases, ilemenite ($FeTiO_3$) [28, 29] as separate phases were also found in iron doped $TiO_2$ photocatalysts. However, the synthesis conditions and the choice of iron precursor strongly influence the evolution of separate iron oxide phases in highly iron loaded $TiO_2$ samples. For example, Tronc et al. [30] synthesized iron/titanium nanoparticles by sol-gel procedure in an inert atmosphere using Ti(IV)-isopropoxide, $FeSO_4 \cdot 7H_2O$ and polyethyleneglycol (PEG) as starting chemicals. Relatively high iron doped $TiO_2$ samples (5 and 15 mol%) contained poorly crystallized hydrated iron(II)-sulphates or basic iron(III)-sulphates in a considerably amount.

In the present work, a series of iron/titanium oxide nanocrystalline particles with Fe/Ti molar ratios of up to 0.15 was synthesized by a modified sol-gel procedure. Ti(IV)-isopropoxide and anhydrous Fe(II)-acetate were used as the precursors of titanium and iron. The precursors were mixed and subsequently hydrolyzed with water molecules generated *in situ* by an esterification reaction between acetic acid and alcohol. Absolute ethanol and glacial acetic acid were additionally purified in order to eliminate the traces of water present in commercial chemicals. This synthesis route differs from those found in the literature and has some advantages such as: (i) synthesis in an inert atmosphere without the traces of water found in commercial chemicals, (ii) iron is introduced in the form of $Fe^{2+}$, (iii) mixing of Ti(IV) and Fe(II) precursor *prior* to hydrolysis, (iv) hydrolysis with water molecules generated *in situ* and (v) compatible titanium and iron organic precursor that is achieved by chemical modification with acetate. The hydrolysis of metal alkoxide by the water molecule generated through an esterification reaction [31–33], as well as the chemical modification of metal alkoxide with acetate [34–36] were reported in the literature; however, these two reactions have never been used to prepare iron doped $TiO_2$ powders. Chemical modification with acetic acid could be advantage in comparison to the modification with acetylacetonate because the acetate group is weaker chelating ligand than acetylacetonate. In addition, iron(III)-acetylacetonate as precursor for the synthesis of iron/titanium oxide particle has been extensively exploited in the literature [8, 22, 25, 26, 37–39].

In a previous study [40] it was shown that iron doped $TiO_2$ ultrafine particles possessed excellent photoactivity under UV irradiation in the killing of SCVII cancer cells. Moreover, that study [40] was the first report to employ an iron doped $TiO_2$ photocatalyst to kill cancer cells. It was hypothesized that the enhanced photocatalytic activity of iron doped $TiO_2$ ultrafine particles in the killing of cancer cells in the presence UV irradiation may arise from the dissolution of iron, thus generating additional hydroxyl radicals by means of the photo Fenton and iron catalyzed Haber-Weiss reactions. At this point, we report a modified synthesis route for preparing nanocrystalline iron doped $TiO_2$. The influence of iron on the structural and microstructural properties of nanocrystalline $TiO_2$ was investigated using XRD, DTA/TGA, Raman, and TEM/SEM techniques.

## 2. Experimental

### 2.1. *Synthesis*

Ti(IV)-isopropoxide (97%) and anhydrous Fe(II)-acetate (95%), supplied by Aldrich, were used as received. Absolute ethanol (99.0%) and glacial acetic acid, supplied by Kemika, Zagreb, were additionally purified as follows: A small quantity of absolute ethanol in the presence of extra pure magnesium powder (Merck) with iodine as a catalyst were heated until all the magnesium was converted to magnesium ethoxide. One liter of absolute alcohol was then added and after 3 hours of refluxing the absolute alcohol was distilled off. Traces of water from the glacial acetic acid were removed by adding some acetic anhydride in the presence of a small quantity of $CrO_3$, refluxed for several hours and then fractionally distilled off.

The synthesis was performed in an oil bath using a specially designed all-glass assembly, which consists of a round-bottom boiling glass flask with four necks, glass mixer, water condenser, inlet glass tube to perform $N_2$ bubbling and one ground outer glass joint used for the addition of reagents. All the apparatuses were connected with ground glass joints. The glass mixer was connected at the outer center of the neck joint of the flask and it consisted of a specially designed glass adapter fixed on the mixer and filled with silicon oil in order to prevent any contact between air moisture and the reaction flask. Before bubbling $N_2$ gas into the reaction vessel, extra pure dinitrogen was additionally purified through a pyrogallol trap, conc. $H_2SO_4$ bubbler and then through two tubes with silica gel. The glass apparatuses were dried at 120°C for at least 12 hours before use. The experiment started by stirring Ti(IV)-isopropoxide and extra dry ethanol, to which an appropriate amount of anhydrous Fe(II)-acetate previously dissolved in acetic acid was added. Each of these steps was performed under an extra-dry nitrogen atmosphere. The thus designed experimental setup provided excellent mixing of all the components and synthesis started from the homogeneous clear solution containing no water. Hydrolysis of the thus modified titanium and iron-titanium precursors was performed with water molecules generated *in situ* through an esterification reaction between acetic acid and alcohol [31–34];

$$\mathrm{ROH} + \mathrm{CH_3COOH} \leftrightarrows \mathrm{H_2O} + \mathrm{CH_3COOR}$$

The solution in the reaction vessel was refluxed and stirred constantly at 500 to 1,000 r.p.m. in a nitrogen atmosphere. After 8 and 9 hours of hydrolysis at 70°C, the formed suspension was poured into big Petri dishes and dried in oven at 60°C under static air conditions. The odour of fruit indirectly confirmed the formation of ester. The flow chart of the preparation procedure for the $TiO_2$ and iron doped $TiO_2$ samples and experimental conditions are given in and Scheme 1 and Table 1, respectively. As synthesized samples were calcinated in a tubular furnace in static-air condition with a temperature stability of ±3°C. The notation of samples throughout the text is given in the form T-X-Y, where X stands for the Fe/Ti molar ratio and Y for the calcination temperature. For example, sample T-5-580 stands for iron doped $TiO_2$ sample with the molar ratio $\mathrm{Fe/Ti} = 0.05$ calcinated at 580°C.

### 2.2. *Instrumental Measurements*

The relative concentrations of iron and titanium in the iron doped $TiO_2$ samples were determined using an Atomic Absorption Spectrometer (AAS) manufactured

*Table 1.* Experimental condition for the synthesis of the $TiO_2$ and iron-doped $TiO_2$ samples. As synthesized samples T-0, T-1, T-5 and T-15 were calcinated in a tubular furnace in static-air condition. The notation of samples throughout the text is given in the form T-X-Y, where X stands for the Fe/Ti molar ratio and Y for the calcination temperature.

| Sample | Volume of $(\mathrm{TiO}^i\mathrm{Pr})_4$/ml | Volume of (EtOH)*/ml | Volume of (HOAc)**/ml | $m(\mathrm{Fe(OAc)_2})$**/g | $n$(Fe)/$n$(Ti) | Time of refluxing at 70°C | Time of drying at 60°C/h |
|---|---|---|---|---|---|---|---|
| T-0 | 25 | 50 | 25 | – | – | 8 h 10 min | 45 |
| T-1 | 25 | 50 | 25 | 0.189 | 0.013 | 8 h 20 min | 42 |
| T-5 | 25 | 50 | 25 | 0.783 | 0.053 | 9 h | 66 |
| T-15 | 25 | 50 | 25 | 2.313 | 0.155 | 8 h 30 min | 40 |

*EtOH = $CH_3CH_2OH$, **OAc = $CH_3COO^-$.

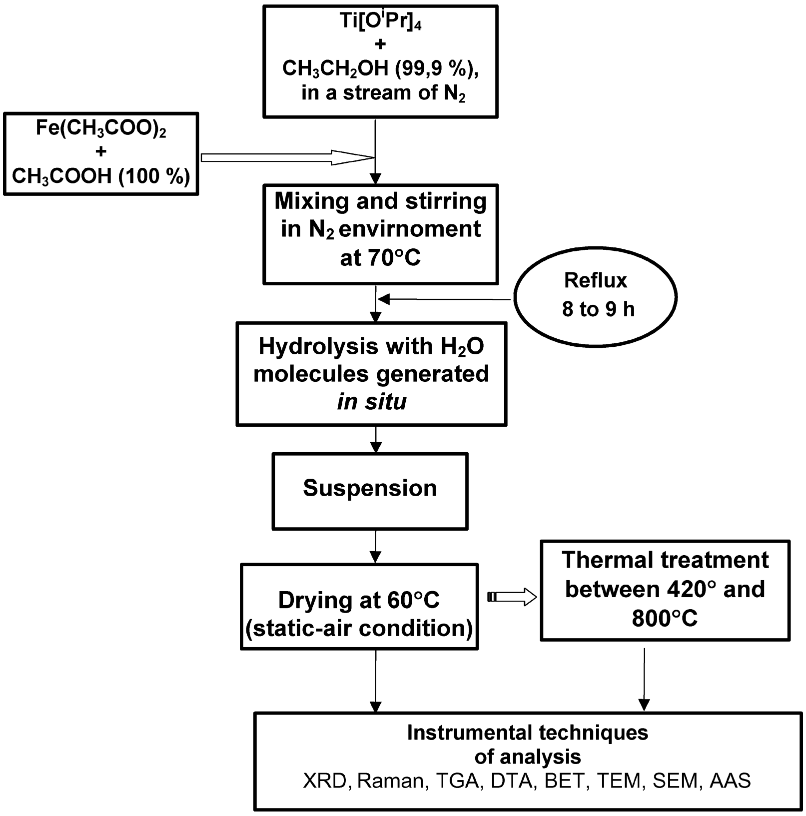

*Scheme 1.* Flow chart of the preparation procedure for $TiO_2$ and Fe-$TiO_2$ powder samples studied in the present work.

by Perkin-Elmer, model 3030B. Powder samples were dissolved and prepared for AAS determinations as follow: ~0.2 g of T-1, T-5 or T-15 samples were finely divided by grinding in an agate mortar and then dissolved in a teflon vial by adding ~5 ml of conc. $H_2SO_4$ and a few drops of conc. hydrofluoric acid until the complete dissolution of the samples was achieved. The reaction is exothermic, and only in the case of the T-15 samples was the teflon vial additionally heated using a sand bath. The dissolved samples were transferred to a plastic bottle and then 100 ml of a 4% solution of $H_3BO_3$ was added in order to eliminate the excess fluoride ions (Solution 1). Furthermore, boric acid prevents the hydrolysis of titanium and iron species, which can occur even in highly acid solutions [41]. For the titanium and iron determinations, 10 ml of Solution 1 was transferred to a 100 ml volumetric flask and diluted to the mark with water treated with Millipore-Milli-Q filtration system. Exceptionally, the solution for the determination of the iron in sample T-1 was prepared by transferring 25 ml

*Table 2.* Comparison of the Fe/Ti molar ratios in the Fe-$TiO_2$ samples calculated from the initially added iron and titanium (nominal values) with those experimentally determined using Atomic Absorption Spectroscopy (AAS).

| | Nominal values | | | Measured values-AAS | | |
|---|---|---|---|---|---|---|
| Sample | $n$(Ti)/mol | $n$(Fe)/mol | $n$(Fe)/$n$(Ti) | $\gamma$(Ti)/$\mu$g ml$^{-1}$ | $\gamma$(Fe)/$\mu$g ml$^{-1}$ | $n$(Fe)/$n$(Ti) |
| T-1 | 0.08147 | 0.00103 | 0.013 | 63.57 | 0.87 | 0.012 |
| T-5 | 0.08147 | 0.00428 | 0.053 | 59.03 | 3.65 | 0.053 |
| T-15 | 0.08147 | 0.01263 | 0.155 | 49.03 | 7.77 | 0.136 |

of Solution 1 to a 50 ml volumetric flask and diluting it to the mark with water treated with Millipore-Milli-Q filtration system. In each solution, 0.1 g of KCl or 0.2 g of $CaCl_2$ was added in order to improve the sensitivity of the titanium and iron, respectively. Standard AA solutions of titanium and iron were prepared using $TiCl_4$ (Cat. No. 092485) and Fe (Cat. No. 121685) Atomic Absorption Standards, as supplied by Aldrich. One linear calibration curve for titanium and two linear calibration curves for iron were prepared using three AA standard aliquots diluted with 4% boric acid.

A comparison of the initially added concentrations of iron and the relative iron concentrations determined using AAS in the iron doped $TiO_2$ samples is given in Table 2.

X-ray powder diffraction (XRD) patterns were taken at room temperature using a Philips counter diffractometer, model MPD 1880 (Cu $K_\alpha$ radiation, graphite monochromator, proportional counter).

The Raman scattering experiments were performed using a standard instrumental technique. A Coherent Innova-100 laser with $\lambda = 514.5$ nm served as the excitation source and the scattered light was analyzed with a DILOR Z-24 Raman spectrometer.

Thermal analysis was performed using an instrument manufactured by Netzsch. The temperature was controlled using a Pt-PtRh (10%) thermocouple, by applying a heating rate of 10°C min$^{-1}$ (DTA) and 5°C min$^{-1}$ (TGA).

The specific surface areas by Brunauer-Emmet-Teller (B.E.T.) were measured using a FlowSorb II 2300 (Micromeritics, USA) analyzer.

Transmission electron microscopy (TEM) was performed with an EM-10 Opton electron microscope. Scanning electron microscopy (SEM) was performed using a PHILIPS instrument with a maximum voltage of up to 20 kV. Samples were prepared by placing their powders onto a conductive graphite strip without making a gold coating.

## 3. Results and Discussion

### 3.1. X-Ray Diffraction

As synthesized, the $TiO_2$ and iron doped $TiO_2$ samples were amorphous for XRD, whereas the amorphous powder precursors started to crystallize after heating to over 300°C. Figure 1 shows the characteristic parts of the X-ray powder diffraction patterns of the $TiO_2$ and iron doped $TiO_2$ samples calcined at 500°C. Sample T-0-500 and T-1-500 were a two-phase mixture of anatase (dominant phase) and rutile (minor phase). The highly iron doped $TiO_2$ samples, samples T-5-500 and T-15-500, were a three-phase system after heating at the same temperature. These samples contained anatase, rutile and a small fraction of an unidentified phase. An approximate determination of the molar fraction of rutile in an undoped $TiO_2$ sample and iron doped $TiO_2$ samples calcined at 500°C (Table 3) indicated a decreased rutile fraction with iron doping.

For the samples calcined at 500°C (Fig. 1), the average crystallite size of anatase decreased from 21 nm in sample T-0-500 to 10 nm in sample T-15-500, as estimated using the Scherrer equation

$$D = 0.9\lambda/(\beta \cdot \cos\theta),$$

where $\lambda$ is the X-ray wavelength, $\theta$ is the Bragg angle and $\beta$ the pure full width of the diffraction line at half of the maximum intensity. The decrease of primary crystallite size with the increasing relative amount of iron in the $TiO_2$ samples was in accordance with the specific surface areas measured by B.E.T., which in the above-mentioned samples increased from 28.4 for the undoped sample to 77.8 m$^2$ g$^{-1}$ for the highest iron doped $TiO_2$ sample, calcined at 500°C (Table 3). The average crystallite size calculated from XRD line broadening and the mean particle size measured from the TEM micrographs (see TEM paragraph) are also

*Table 3.* XRD phase analysis, BET specific surface areas, XRD crystallite size and TEM mean particle size of undoped $TiO_2$ and iron-doped $TiO_2$ samples.

| Sample | XRD phase analysis (approximate molar fraction) | XRD crystallite size of dominant component (esd)[a]/nm | TEM mean particle size (sd)[b]/nm | BET specific surface areas/ $m^2g^{-1}$ |
|---|---|---|---|---|
| T-0 | Amorphous | – | | 1.54 |
| T-0-500 | A + R (0.10) | 21(5) | 16.3(3.4) | 28.47 |
| T-0-580 | R + A (0.03) | >100 | | 2.30 |
| T-0-800 | R | >100 | | 5.13 |
| T-1 | Amorphous | – | | 2.67 |
| T-1-500 | A + R (0.05) | 17(4) | 16.2(3.9) | 43.77 |
| T-1-580 | R + A (0.08) | 49(10) | | 4.19 |
| T-1-800 | R | 85(20) | | 3.26 |
| T-5 | Amorphous | – | | 4.84 |
| T-5-500 | A + R (0.05) + X (small amount) | 12(2) | 11.5(1.8) | 66.57 |
| T-5-580 | R + A (0.50) | 19(4) | | 24.07 |
| T-5-800 | R + PB (0.05) | 60(12) | | 6.07 |
| T-15 | Amorphous | – | | 3.74 |
| T-15-420 | A + R (0.03) + X (small amount) | 9(1) | | 102.30 |
| T-15-500 | A + R (0.05) + X (small amount) | 10(2) | 9.7(1.5) | 77.80 |
| T-15-580 | R + H(0.05) + A (0.03) | 19(4) | | 18.76 |
| T-15-800 | R + PB (0.7) | 80(15) | | 7.05 |

*Key*: [a]esd = estimated standard deviation, [b]sd = mean particle size and standard deviation were calculated using normal function (see also TEM paragraph), A = anatase, *R* = rutile, PB = pseudobrookite, H = hematite, X = unidentified phase.

shown in Table 3. The values of these two measurements are in a very good agreement.

Figure 2 shows characteristic parts of the X-ray powder diffraction patterns of the $TiO_2$ and iron doped $TiO_2$ samples calcined at 580°C. Sample T-0-580 and T-1-580 consisted of rutile as the dominant phase and a minor amount of anatase. The relative amount of anatase was higher in sample T-1-580 than in an undoped $TiO_2$ sample. Moreover, the approximate molar fraction of anatase increased with iron doping to a surprising 50 mol% in sample T-5-580 . The highest iron doped sample, T-15-580, showed different structural behavior due to unambiguous iron segregation. This sample was a three-phase system with rutile as the dominant phase and a small fraction of hematite and anatase. The average crystallite size of the dominant component in the samples calcined at 580°C, as determined using the Scherrer equation, decreased from >100 nm in an undoped sample to 19 nm in the highest iron doped sample. It is evident that the iron-doping prevented the crystal growth of the dominant component in iron doped $TiO_2$ samples.

Samples T-0-800 and T-1-800 consisted of rutile, whereas highly iron doped $TiO_2$ samples were two-phase mixtures of rutile and pseudobookite, $Fe_2TiO_5$. The relative amount of pseudobrookite in the highly iron doped samples increased with iron doping (Table 3).

The XRD results of the present study showed an unidentified phase in samples T-5-500 and T-15-500 that was neither a titanium oxide nor an iron oxide and a titanium-iron oxide. This finding undoubtedly differed from those of other investigations that considered the presence of hematite or pseudobrookite as the only segregated iron phases in iron doped $TiO_2$ powder samples. The appearance of the new phase with

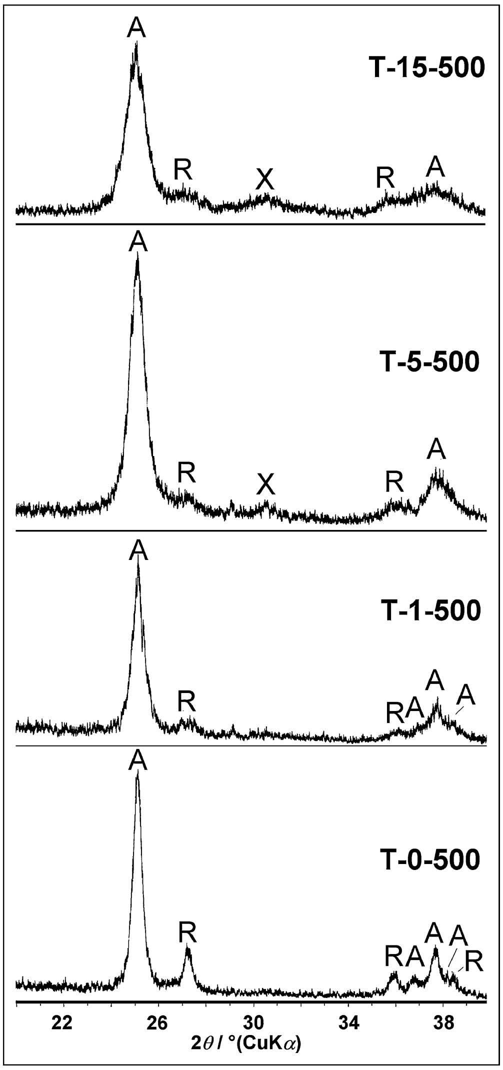

*Figure 1.* Characteristic parts of the X-ray powder diffraction patterns of the TiO$_2$ and iron-doped TiO$_2$ samples calcined at 500°C (A-anatase, R-rutile, X-unidentified phase).

the diffraction maximum at $2\theta = 30.8^\circ$ (Cu $K_\alpha$ radiation) could be influenced by the novel synthesis route using to prepare iron doped TiO$_2$ nanocrystalline particles. The synthesis conditions (inert atmosphere) and the choice of iron(II) precursor strongly influenced the evolution of separate iron oxide phases during the calcination in the static-air conditions. Therefore, all further investigations of iron doped TiO$_2$ (with molar ratio Fe/Ti $\geq$ 0.05) performed under similar synthesis conditions, as shown in the present work, should search not only for pseudobrookite or hematite, but also for additional iron/titanium oxide-related phases.

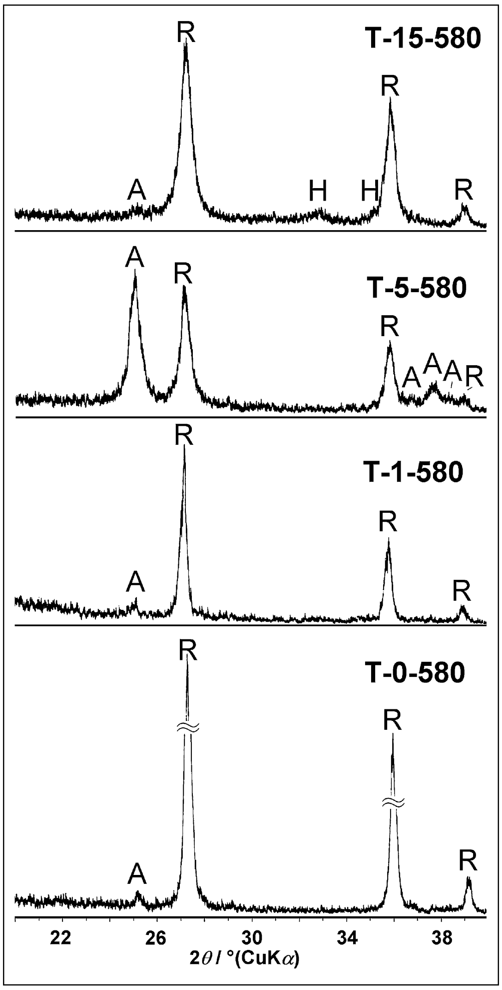

*Figure 2.* Characteristic parts of the X-ray powder diffraction patterns of the TiO$_2$ and iron-doped TiO$_2$ samples calcined at 580°C (A-anatase, R-rutile, H-hematite).

### *3.2. Thermal Analysis*

The results of the thermogravimetric analysis (TGA) of samples T-0, T-1, T-5 and T-15 are shown in Fig. 3. All samples permanently loss on weight from RT to about 400°C; however, the slight discontinuous in TGA traces between RT and 100°C, 100 and 200°C and 200 and 400°C are noticed. In the region from RT to 100°C, the evaporation of solvents occurred. In the region between 100 and about 200°C, there was thermal degradation of the loosely bound organics. Finally, the tightly bound organic residues were thermally decomposed above 200°C. The weight loss started from RT and completed at about 400°C, which depended on

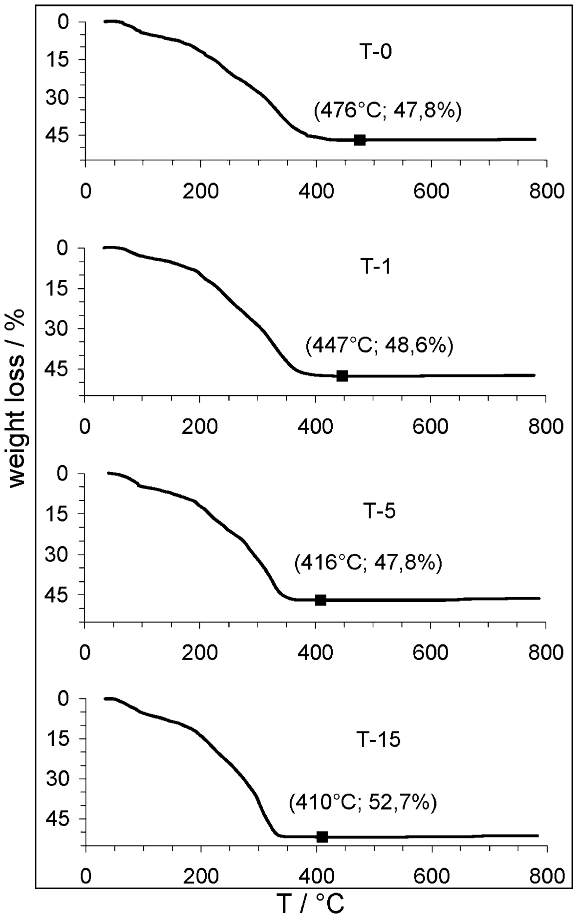

*Figure 3.* TGA curves of undoped $TiO_2$ sample T-0 and iron-doped $TiO_2$ samples, T-1, T-5 and T-15. Heating of the samples in static-air conditions started from the RT by applying a heating rate of 5°C $min^{-1}$. The square in the TGA curves shows the point at which constant weight loss was reached.

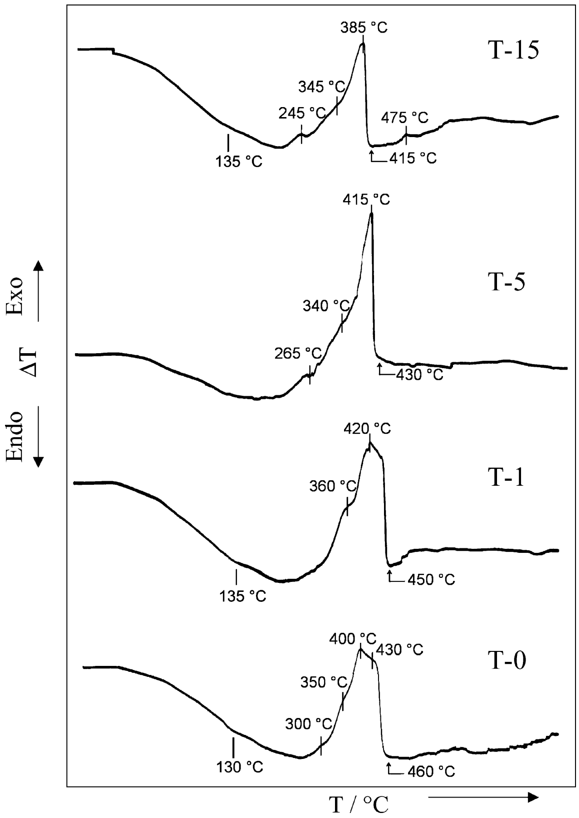

*Figure 4.* DTA curves of undoped $TiO_2$ sample T-0 and iron-doped $TiO_2$ samples T-1, T-5 and T-15. Heating of the samples in static-air conditions started from the RT by applying a heating rate of 10°C $min^{-1}$. The scale of the heating rate is not linear.

the relative doped iron content in the Fe-$TiO_2$ sample. Clearly, as the relative concentration of iron in the Fe-$TiO_2$ samples increased, weight loss occurred at lower temperatures. For example, the total weight losses of 47.8 wt% reached at 476°C and 52.70 wt% reached at 410°C were respectively found for an undoped sample, T-0, and a highly iron doped sample, T-15.

Figure 4 shows the results of differential thermal analysis (DTA). The DTA curve of undoped sample T-0 is characterized by endothermic shoulder at 130°C and a series of not well resolved exothermic peaks with maximums at about 400 to 430°C. The endothermic shoulder at 130°C could be ascribed to the evaporation of solvents. The exothermic effect at 400–430°C with two other poorly resolved exothermic shoulders at 300 and 350°C correspond to the amorphous-anatase transition. This process is quite complex for high surface area powders and includes several steps such as the thermal degradation of tightly bound organic molecules, the additional condensation of unhydrolyzed —OR groups, the sintering and growth of particles and the structural rearrangement of newly formed Ti—O bonds [42, 43].

With the addition of iron to $TiO_2$, the exothermic peak in the DTA curve shifted to lower temperatures. Furthermore, the exothermic peak in the DTA curve became much more asymmetric and completed more steeply to the higher-temperature side as the fraction of iron increased. This effect is clearly visible in the DTA curve of sample T-5, where the exothermic peak rises asymmetrically and goes down the most steeply. Kumar et al. [44] explained the asymmetric broadening of the exothermic peak to the low-temperature side by the heat release that starts before the actual grain growth. This type of asymmetric exotherm is typical of grain growth initiated by phase transition. It can be concluded that iron speeded up the thermal decomposition of loosely and tightly bound organic molecules and, consequently, the amorphous-to-anatase transition was completed at a lower temperature.

A new exothermic peak at 265°C appeared in the sample T-5. This peak is more intense in sample T-15 (245°C). This new peak could be explained by the influence of iron, which in higher concentration strongly influence the thermal history of iron doped $TiO_2$ samples.

### *3.3. Raman Spectroscopy*

$TiO_2$ polymorphs have been extensively studied by Raman spectroscopy [45–54]. In addition, low-frequency Raman spectroscopy has been successfully applied to $TiO_2$ particle size determination [34, 55–58]. On the other hand, iron doped $TiO_2$ has not been extensively studied by Raman spectroscopy. Bersani et al. [59] studied the iron-titanium mixed oxides produced by the sol-gel method using micro-Raman spectroscopy. An overall broadening of the Raman peaks of anatase and rutile was observed with increasing iron content. This effect was explained by increased disorder due to the inclusion of iron ions in the titania network or by the lower size of the titania nanocrystals due to the presence of iron impurities at the grain boundaries, which slowed the growth of titania grains. Pseudobrookite was the only crystalline phase found, involving both iron and titanium. A definite trend with the amount of the dopant was not observed for the anatase-to-rutile transition temperature.

Wang et al. [60] synthesized Fe(III)-doped titania powders using a flame aerosol reactor. It was found that at low Fe:Ti ratios (<0.12), the mode frequencies compared favorably to those of pure anatase. At higher Fe:Ti ratios (>0.4), significant mode frequency shifts were observed. An increased shift and broadening of the anatase Raman peaks with increasing iron concentration was attributed to shrinkage in the grain size. Furthermore, with increased iron concentration, a decrease in the crystal size of the resultant titania particles was observed together with a conversion to the amorphous state. The iron incorporated into the titania lattice promoted the conversion of anatase to rutile.

Figure 5 shows Raman spectra of $TiO_2$ and iron doped $TiO_2$ samples calcined at 500°C. In the iron doped samples, there are no bands belonging to rutile; only the undoped $TiO_2$ sample, T-0-500, contains two bands of rutile at 612 and 447 $cm^{-1}$ of very small relative intensities. These results are in very good agreement with the XRD results. The bands at 362, 312 and 250 $cm^{-1}$ belong neither to rutile nor anatase, so the origin of these bands could be correlated with iron doping. The most intense Raman band of anatase at about 143 $cm^{-1}$ shifted from 143.8 in an undoped $TiO_2$ sample to 149.6 $cm^{-1}$ in the highest iron doped sample, T-15-500.

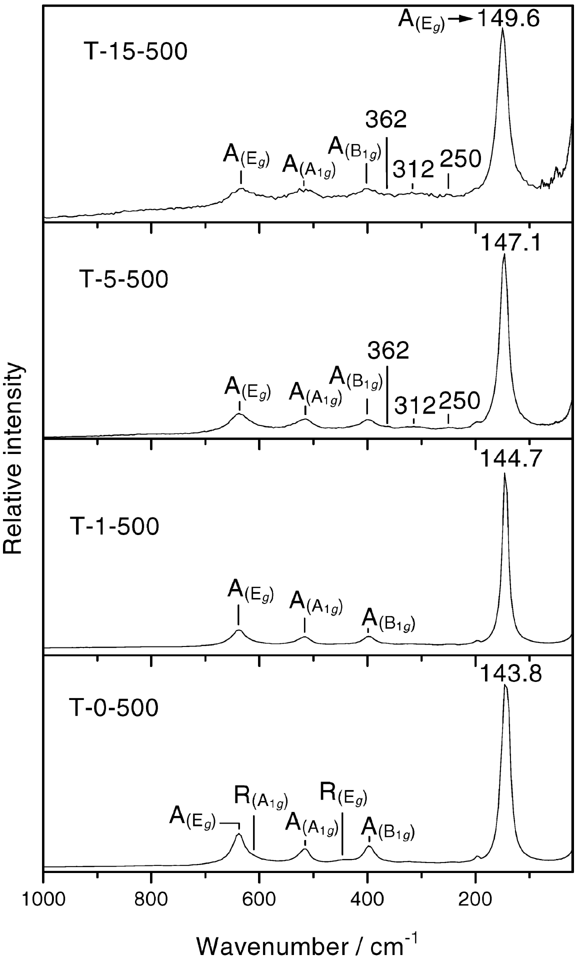

*Figure 5.* Raman spectra recorded in the wave number range from 1,000 to 20 $cm^{-1}$ of $TiO_2$ and iron-doped $TiO_2$ samples calcined at 500°C (A-anatase, R-rutile; the active Raman fundamentals of anatase and rutile given in brackets).

Figure 6 shows Raman spectra of $TiO_2$ and iron doped $TiO_2$ samples calcined at 580°C. The Raman spectrum of the highest iron doped sample, T-15-580, is not shown because of the poor quality and flattened bands of the Raman spectrum, due to the high absorption and fluorescence of iron in this spectral region. The undoped $TiO_2$ sample, T-0-580, consisted of rutile and

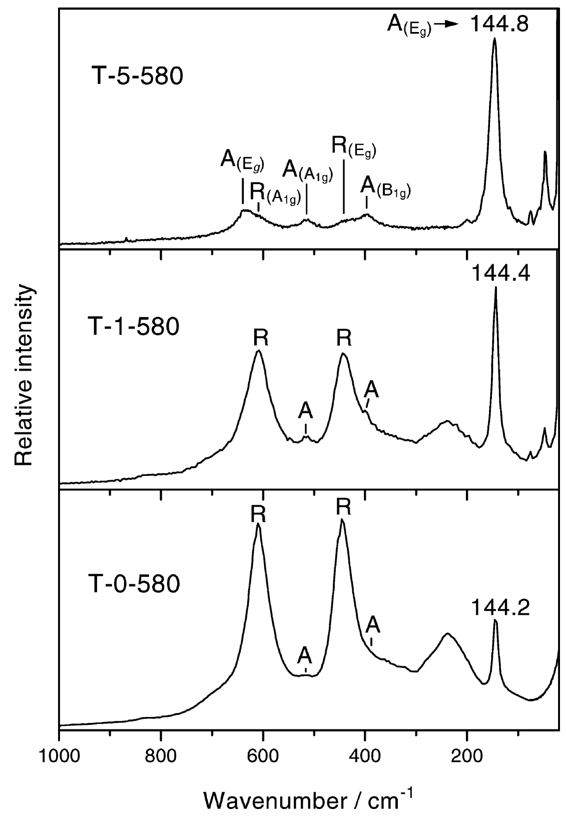

*Figure 6.* Raman spectra recorded in the wave number range from 1,000 to 20 cm$^{-1}$ of TiO$_2$ and iron-doped TiO$_2$ samples calcined at 580°C (A-anatase, R-rutile; the active Raman fundamentals of anatase and rutile given in brackets).

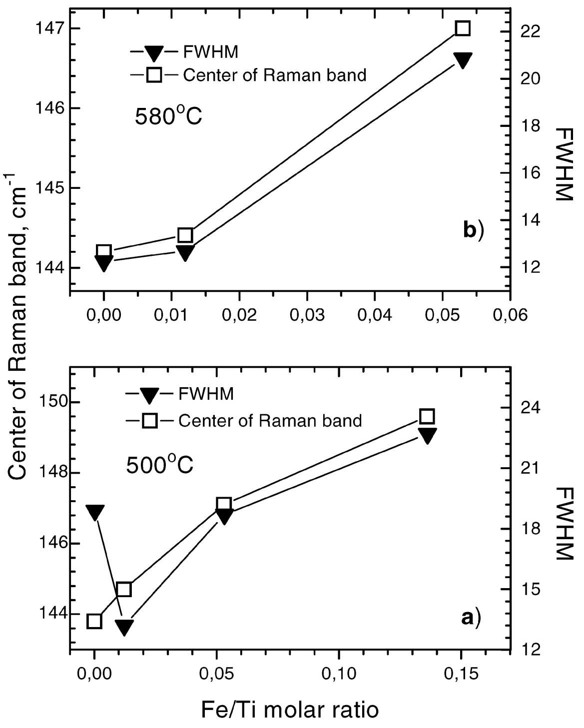

*Figure 7.* The dependence of the center of the most intensive Raman band of anatase at ~144 cm$^{-1}$ ($E_g$ mode) and the full width at half maximum (FWHM) of the same Raman band with the Fe/Ti molar ratio in iron-doped TiO$_2$ samples after thermal treatments at 500°C (a) and 580°C (b). Anatase bands at ~144 cm$^{-1}$ were fitted to the Lorentzian curve profile. Due to the strong fluorescence of the highest iron-doped TiO$_2$ sample after thermal treatment at 580°C, the Raman band at 144 cm$^{-1}$ was not well developed and thus not considered.

a small quantity of anatase. With increased iron doping, the relative amounts of anatase increased, which can be seen from (a) the increased relative intensities of the anatase bands at 520, 405 and ~144 cm$^{-1}$, (b) the decreased relative intensities of the rutile bands at 610 and 447 cm$^{-1}$, and (c) the development of the anatase band at 638 cm$^{-1}$ in the iron doped sample, T-5-580. These results are in a very good agreement with the XRD results, which showed that the relative amount of anatase increased with iron doping and that the sample T-5-580 consisted of about 50 mol% of anatase.

Figure 7 shows the shift of the center of the most intense Raman band of anatase at 144 cm$^{-1}$ ($E_g$ mode) and its broadening with iron doping. It is clearly visible that the center of the Raman band of the $E_g$ mode continuously shifted to higher wave numbers with increased iron doping for both calcination temperatures at 500 and 580°C. Also, the full width at half maximum (FWHM) increased with iron doping. The exception is the value of the FWHM of the undoped sample T-0-500 calcined at 500°C. This sample showed a higher FWHM than the iron doped sample T-1-500, very probably due to the presence of rutile and the more difficult degradation of the organic phase in the undoped sample. The shift of the center of the Raman band at ~144 cm$^{-1}$ and its broadening with increased iron doping could be explained by increased disorder induced by the presence of iron or by the phonon confinement effect that dominated with decreasing of the mean nanoparticle sizes. The iron species at the grain boundaries may slow the growth of titania grains and/or become incorporated in the TiO$_2$ network. This is not in contradiction with the thermal analysis results, which showed the acceleration and shifting of the amorphous-to-anatase transition to lower temperature values with iron doping. Once grains of anatase were formed, the iron at the grain boundaries may inhibit grain growth.

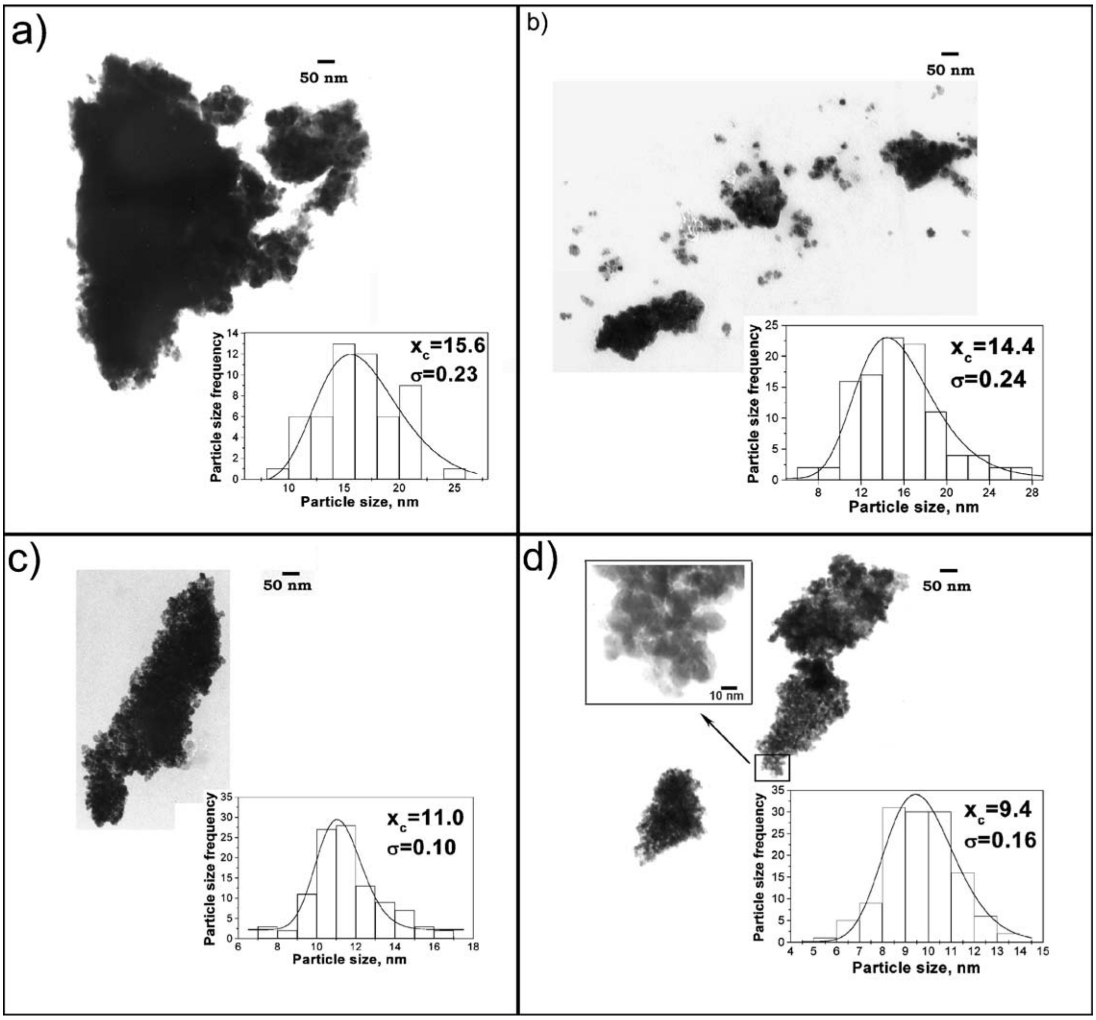

*Figure 8.* Transmission electron micrographs of samples T-0-500 (a), T-1-500 (b), T-5-500 (c) and T-15-500 (d) with the attached particle size distributions. Particle size distribution was calculated using LogNormal function($y = y_0 + Ae^{\frac{\ln^2(x/x_c)}{2\sigma^2}}$). The peak of distribution, $x_c$, decrased from $x_c = 15.6$ nm in sample T-0-500 to $x_c = 9.4$ nm in sample T-15-500. The $\sigma$ parameter in LogNormal function, related to the distribution width, decreased from $\sigma = 0.23$ in sample T-0-500 to $\sigma = 0.10$ in sample T-5-500 and than slightly increase to $\sigma = 0.16$ in sample T-15-500. The narrowest, monochromatic, particle size distribution was found in sample T-5-500. An enlarged detail of micrograph of sample T-15-500 is attached as inset in Fig. 8(d) that one can see very small segregated particles with diameter about 1 nm dispersed on the bigger particles.

### 3.4. *Transmission Electron Microscopy (TEM)*

Figure 8 shows the transmission electron micrographs with the attached particle size distributions of the samples calcined at 500°C. Particle size distribution was calculated using LogNormal function. Sample T-0-500 consists of particles about 15.6 nm organized in large irregular compact aggregates. The distinct particles are visible at the periphery of aggregates. With iron doping compact aggregates become more "transparent" and consequently, the distinct particles in the middle of the aggregates are visible (Fig. 8(d)). Further, with iron doping the irregular and relatively big particles changed to more uniform and smaller particles. The peak of LogNormal distribution decreased from 15.6 nm in undoped sample (Fig. 8(a)) to 9.4 nm in the highest iron doped sample (Fig. 8(d)). Also, the particle size distribution becomes narrower with iron doping. The $\sigma$ parameter ($\sigma$ parameter in LogNormal function is related to the distribution width) decreased from $\sigma = 0.23$ in

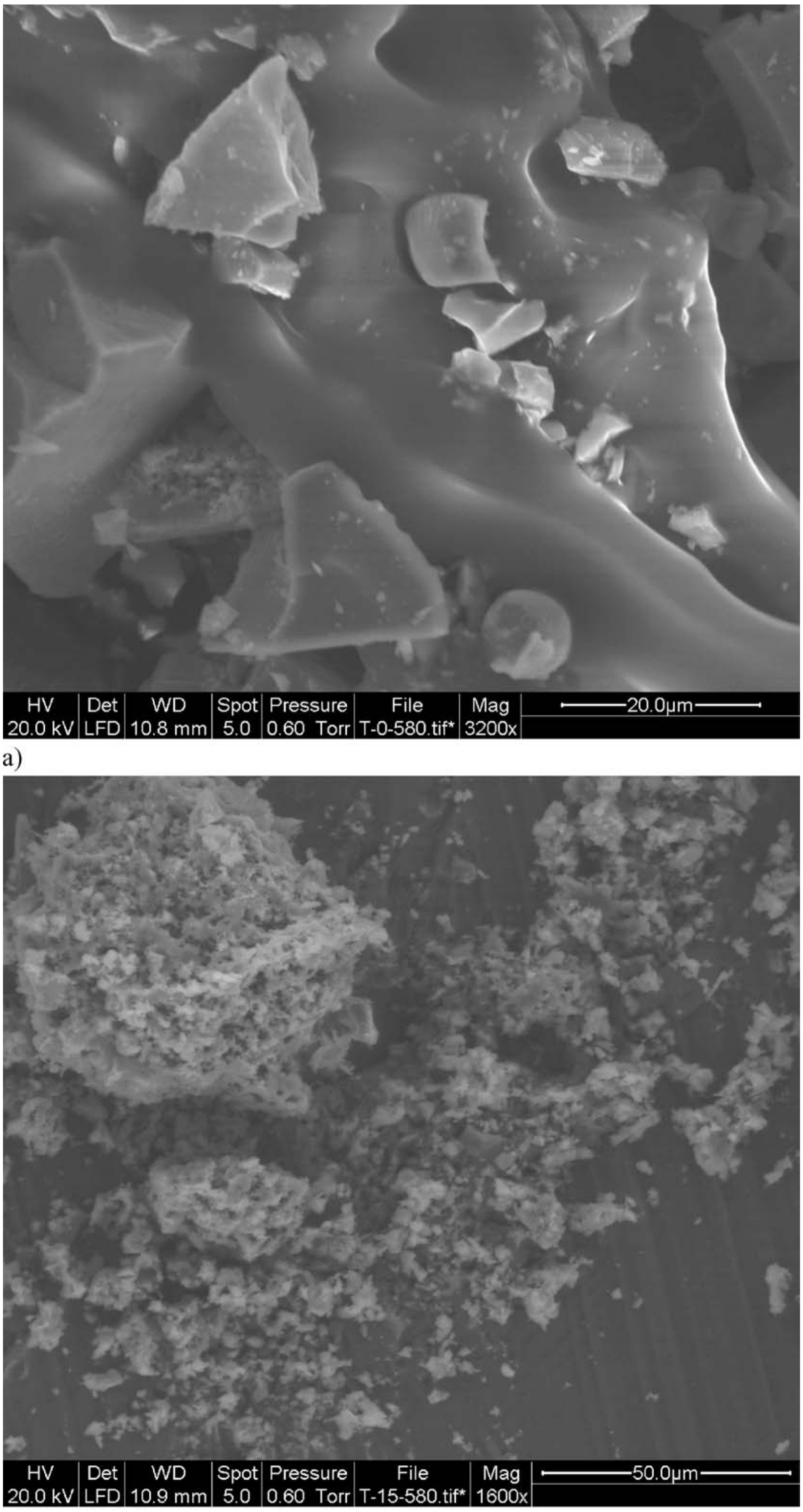

a)

b)

*Figure 9*. Scanning electron micrographs obtained by analyzing a powder of sample T-0-580 (a) and sample T-15-580 (b).

sample T-0-500 to $\sigma = 0, 10$ in sample T-5-500 and than slightly increase to $\sigma = 0, 16$ in sample T-15-500. Therefore the narrowest, monochromatic, particle size distribution was found in sample T-5-500. It should be pointed here that position of the peak in LogNormal function do not correspond exactly to the mean particle size and because of that the values given in Table 3 differs from the $x_c$ values given in Fig. 8.

On the basis of the experimental results shown, it is not possible to conclude whether the single particle is multicomponent, or the sample is a mixture of several kinds of particles having different compositions. However, by enlarging the micrograph (Fig. 8(d)) one can see very small segregated particles with diameter about 1 nm dispersed on the bigger 10 nm particles in sample T-15-500. These 1 nm particles in sample T-15-500 might belong to the separated unidentified iron oxide-related phase.

In a previous work [40], we showed that the highly iron doped $TiO_2$ particles investigated in the present work possessed an excellent photoactivity in the killing of SCVII cancer cells under UV irradiation. It was hypothesized that the enhanced photocatalytic activity of highly iron doped $TiO_2$ samples may arise from dissolution of iron, thus generating additional hydroxyl radicals by means of the photo Fenton and iron catalyzed Haber-Weiss reaction. From the microstructural standpoint, the better photocatalytic activity of highly iron doped $TiO_2$ samples might be explained by the affirmative balance between particle size and degree of crystallinity, narrower particle size distribution, "softer" aggregates with more distinct particles and higher specific surface areas.

### 3.5. *Scanning Electron Microscopy (SEM)*

Figure 9 shows the scanning electron micrographs of the samples T-0-580 (a) and T-15-580 (b). Sample T-0-580 consists of small irregular aggregates of various sizes and shapes with noticeable edges and flat faces adhering to the smooth relief surface of large aggregate. In contrast, an iron doped $TiO_2$ sample consists of small and large aggregates of expressive porous surface.

The SEM results showed a remarkable influence of iron on the morphology of the iron doped $TiO_2$ samples. Doping with iron changes the flat surfaces in the undoped $TiO_2$ samples to highly porous, sponge-like surfaces in the iron doped $TiO_2$ samples after thermal treatment at the same temperatures. The effect was also observed in the other iron doped $TiO_2$ samples calcinated at 500 and 800°C (micrographs are not shown). This effect could be explained by the role of iron that catalyzes the thermal degradation and oxidation of organic molecules to $CO_2$. Carbon dioxide is generated by the decomposition and oxidation of the organic residue diffused to the surface and desorbed from the surface [15], thus developing porous, sponge-like structures with uniformly distributed micrometer holes.

## 4. Conclusions

$TiO_2$ and iron doped $TiO_2$ nanosized particles were synthesized by a modified sol-gel procedure starting from an organic precursor completely in an organic medium in extra dry surroundings. The sources of the titanium and iron were Ti-isopropoxide and anhydrous Fe(II)-acetate. Homogeneous hydrolysis of the titanium and iron precursors was performed by water molecules generated *in situ* by an esterification reaction between alcohol and acetic acid.

Iron-doping accelerated the thermal degradation of the organic residues in the Fe-$TiO_2$ samples. The relatively flat surfaces of the undoped $TiO_2$ particle aggregates changed to sponge-like surfaces with rather uniformly distributed micrometer holes.

With increased iron doping, the average crystallite size of the dominant phase in Fe-$TiO_2$ samples decreased, whereas the BET surface area of the Fe-$TiO_2$ particles increased. Furthermore, the particle size decreased and the particle size distribution became narrower with iron doping.

With increased iron doping, the relative amount of anatase in the iron-doped $TiO_2$ samples increased for the samples thermally treated at 500°C and 580°C. As a consequence, quite unexpectedly, an extremely high amount of anatase fraction (50 mol% of anatase) in the iron doped $TiO_2$ sample thermally treated at 580°C was possible.

Iron that could not be incorporated in the $TiO_2$ matrix separated at a lower heating temperature (up to 500°C) in the form of an unidentified phase, or at higher heating temperatures (580°C), in the forms of hematite ($\alpha$-$Fe_2O_3$) and pseudobrookite ($Fe_2TiO_5$).

The excellent photoactivity of these iron doped $TiO_2$ ultrafine particles under UV irradiation in the killing of SCVII cancer cells shown in a previous work [40] might be explained in part by specific microstructural properties described in the present work.

## Acknowledgments

The authors wish to thank prof. Nikola Ljubešić for his assistance with electron microscopy, dr. Rudolf Trojko for performing TGA/DTA measurements and Mr. Srečko Karašić for performing BET measurements.

## References

1. T. Chafik, A.M. Efstathiou, and X.E. Verykios, J. Phys. Chem. B **101**, 7968 (1997).
2. F. Milella, J.M. Gallardo-Amores, M. Baldi, and G. Busca, J. Mater. Chem. **8**, 2525 (1998).
3. C. Lettmann, H. Hinrichs, and W.F. Maier, Angew. Chem. Int. Ed. **40**, 3160 (2001).
4. G.N. Schrauzer and T.D. Guth, J. Am. Chem. Soc. **99**, 7189 (1977).
5. L. Palmisano, V. Augugliaro, A. Sclafani, and M. Schiavello, J. Phys. Chem. **1988**, 6710 (1988).
6. J. Soria, J.C. Conesa, V. Augugliaro, L. Palmisano, M. Schiavello, and A. Sclafani, J. Phys. Chem. **95**, 274 (1991).
7. W. Choi, A. Termin, and M.R. Hoffmann, J. Phys. Chem. **98**, 13669 (1994).
8. C.-Y. Wang, D.W. Bahnemann, and J.K. Dohrmann, Chem. Commun. 1539 (2000).
9. D. Bockelmann, M. Lindner, and D. Bahnemann, in *Fine Particles Science and Technology*, edited by E. Pelizzetti (Kluwer Academic Publishers, Dordrecht, The Netherlands, 1996), p. 675.
10. J. Araña, O. González Díaz, M. Miranda Saracho, J.M. Doña Rodríguey, J.A. Herrera Melián, and J. Pérey Peña, Appl. Catal. B: Eviron. **32**, 49 (2001).
11. J. Araña, O. González Díaz, M. Miranda Saracho, J.M. Doña Rodríguey, J.A. Herrera Melián, and J. Pérey Peña, Appl. Catal. B: Eviron. **36**, 113 (2002).
12. K.T. Ranjit, I. Willner, S. Bossmann, and A. Braun, J. Phys. Chem. B **102**, 9397 (1998).
13. A.B. Rivas, T.S. Kulkarni, and A.L. Schwaner, Langmuir **9**, 192 (1993).
14. Y. Wang, H. Cheng, Y. Hao, J. Ma, W. Li, and S. Cai, J. Mater. Sci. **34**, 3721 (1999).
15. K. Kato, A. Tsuge, and Ko-ichi Niihara, J. Am. Ceram. Soc. **79**, 1483 (1996).
16. D. Cordischi, N. Burriesci, F. D'Alba, M. Petrera, G. Polizzotti, and M. Schiavello, J. Solid State Chem. **56**, 182 (1985).
17. J.S. Thorp, H.S. Eggleston, T.A. Egerton, and A.J. Pearman, J. Mater. Sci. Lett. **5**, 54 (1986).
18. R.I. Bickley, J.S. Lees, R.J.D. Tilley, L. Palmisano, and M. Schiavello, J. Chem. Soc. Faraday Trans. **88**, 377 (1992).
19. R.I. Bickley, T. Gonzalez-Carreño, A.R. Gonzalez-Elipé, G. Munuera, and L. Palmisano, J. Chem. Soc. Faraday Trans. **90**, 2257 (1994).
20. U. Schwertmann, J. Friedl, G. Pfab, and A.U. Gehring, Clays & Clay Miner. **43**, 599 (1995).
21. M.V. Tsodikov, O.V. Bukhtenko, O.G. Ellert, V.M. Shcherbakov, and D.I. Kochubey, J. Mater. Sci. **30**, 1087 (1995).
22. J. A. Navío, G. Colón, M. Macías, C. Real, and M.I. Litter, Appl. Catal. A **177**, 111 (1999).
23. Yu-H. Zhang and A. Reller, J. Mater. Chem. **11**, 2537 (2001).
24. J.A. Wang, R. Limas-Ballesteros, T. Lopez, A. Moreno, R. Gomez, O. Novaro, and X. Bokhimi, J. Phys. Chem. B **105**, 9692 (2001).
25. P. Guglielmi and P. Colombo, Cer. Acta **1**, 19 (1989).
26. P. Colombo, M. Guglielmi, and S. Enzo, J. European Ceram. Soc. **8**, 383 (1991).
27. M. Maček, B. Orel, and T. Meden, J. Sol-Gel Sci. Technol. **8**, 771 (1997).
28. Zh. H. Suo, Y. Kou, and H. Wang, Chin. J. Catal. **22**, 348 (2001).
29. N. Smirnova, A. Eremenko, O. Rusina, W. Hopp, and L. Spanhel, J. Sol-Gel Sci. Technol. **21**, 109 (2001).
30. E. Tronc, M. Gotić, S. Musić, M. Ivanda, and S. Popović, unpublished results.
31. H. Schmidt and B. Seiferling, Mat. Res. Soc. Symp. Proc. **73**, 739 (1986).
32. A. Larbot, I. Laaziz, J. Marignan, and J.F. Quinson, J. Non-Crystall. Solids **147/148**, 157 (1992).
33. C.-C. Huang and Chi-Sh. Wu, Journal of The Chin. I. Ch. E. **28**, 61 (1997).
34. S. Doeuff, M. Henry, C. Sanchez, and J. Livage, J. Non-Crystall. Solids **89**, 206 (1987).
35. P. Griesmar, G. Papin, C. Sanchez, and J. Livage, Chem. Mater. **3**, 335 (1991).
36. S. Barboux-Doeuff and C. Sanchez, Mat. Res. Bull. **29**, 1 (1994).
37. J.A. Navío, G. Colón, M.I. Litter, and G.N. Bianco, J. Mol. Catal. **106**, 267 (1996).
38. J.A. Navío, G. Colón, M. Trillas, J. Peral, X. Domènech, J.J. Testa, J. Padrón, D. Rodríguez, and M.I. Litter, Appl. Catal. B **16**, 187 (1998).
39. B. Pal, M. Sharon, and G. Nogami, Mater. Chem. Phys. **59**, 254 (1999).
40. S. Ivanković, M. Gotić, M. Jurin, and S. Musić, J. Sol-Gel Sci. Technol. **27**, 225 (2003).
41. M. Codell, *Analytical Chemistry of Titanium Metals and Compounds* (Interscience Publishers, Inc., New York, Interscience Publishers Ltd., London, 1959), p. 178.
42. J.M. Gallardo Amores, V. Sanchez Escribano, and G. Busca, J. Mater. Chem. **5**, 1245 (1995).
43. R. Rodríguez-Talavera, S. Vargas, R. Arroyo-Murillo, R. Montiel-Campos, and E. Haro-Poniatowski, J. Mater. Res. **12**, 439 (1997).
44. K.-N.P. Kumar, K. Keizer, A.J. Burggraaf, T. Okubo, H. Nagamoto, and S. Morooka, Nature **358**, 48 (1992).
45. I.R. Beattie and T.R. Gilson, J. Am. Chem. Soc. (A) 2322 (1969).
46. S.P. Porto, P.A. Fleury, and T.C. Damen, Phys. Rev. **154**, 522 (1967).
47. J.C. Parker and R.W. Siegel, J. Mater. Res. **5**, 1246 (1990).
48. A. Turković, M. Ivanda, A. Drašner, V. Vraneša, and M. Peršin, Thin Solid Films **198**, 199 (1991).
49. G.A. Tompsett, G.A. Bowmaker, R.P. Cooney, J.B. Metson, K.A. Rodgers, and J.M. Seakins, J. Raman Spectrosc. **26**, 57 (1995).
50. Y. Iida, M. Furukawa, K. Kato, and H. Morikawa, Appl. Spectrosc. **51**, 673 (1997).
51. S. Kelly, F.H. Pollak, and M. Tomkiewicz, J. Phys. Chem. B. **101**, 2730 (1997).
52. D. Bersani, G. Antonioli, P.P. Lottici, and T. Lopez, J. Non-Crystall. Solids **232–234**, 175 (1998).
53. D. Bersani, P. Lottici, and X-Z Ding, Appl. Phys. Lett. **72**, 73 (1998).

54. J. Slunečko, M. Kosec, J. Holc, G. Dražić, and B. Orel, J. Am. Ceram. Soc. **81**, 1121 (1998).
55. M. Gotić, M. Ivanda, A. Sekulić, S. Musić, S. Popović, A. Turković, and K. Furić, Mater. Lett. **28**, 225 (1996).
56. S. Musić, M. Gotić, M. Ivanda, S. Popović, A. Turković, R. Trojko, A. Sekulić, and K. Furić, Mater. Sci. Eng. B **47**, 33 (1997).
57. M. Gotić, M. Ivanda, S. Popović, S. Musić, A. Sekulić, A. Turković, and K. Furić, J. Raman. Spectr. **28**, 555 (1997).
58. M. Ivanda, S. Musić, M. Gotić, A. Turković, A.M. Tonejc, and O. Gamulin, J. Mol. Struct. **480/481**, 641 (1999).
59. D. Bersani, P.P. Lottici, and A. Montenero, J. Mater. Sci. **35**, 4301 (2000).
60. Z.-M. Wang, G.X. Yang, P. Biswas, W. Bresser, and P. Boolchand, Powder Technol. **114**, 197 (2001).